Liquid film thickness of upward air-water annular flow after passing through 90° bend

Kurimoto, Ryo
Takeuchi, Yuji
Minagawa, Hisato
Yasuda, Takahiro

(Citation)
Experimental Thermal and Fluid Science,139:110735

(Issue Date)
2022-11-01

(Resource Type)
journal article

(Version)
Accepted Manuscript

(URL)
https://hdl.handle.net/20.500.14094/0100476312

Liquid film thickness of upward air-water annular flow after passing through 90º bend

Ryo Kurimoto[1*], Yuji Takeuchi[2], Hisato Minagawa[3], Takahiro Yasuda[3]

1 Graduate School of Engineering, Kobe University
1-1, Rokkodai, Nada, Kobe, Japan.
2 Graduate School of Engineering, The University of Shiga Prefecture
2500, Hassaka, Hikone, Shiga, Japan.
3 School of Engineering, The University of Shiga Prefecture
2500, Hassaka, Hikone, Shiga, Japan.

*Corresponding author: kurimoto@mech.kobe-u.ac.jp

Highlights

(1) This paper dealt with upward annular flows after passing through a 90º bend.
(2) Axial development of the base film thickness was discussed.
(3) The axial velocity in the liquid film was measured.

Abstract

Axial development of the base film thickness of an upward air-water annular flow after passing through a 90º bend was investigated. The pipe diameter D of the channel was 5.0 mm. The ratios, R^*, of the radius of curvature of a bend to D were 6.0 and 10. The dimensionless axial distances, z^* (= z/D), of measurement positions were 4, 12 and 20, where z is the axial coordinate in the vertical section. The circumferential measurement positions, θ, from the outer side to the inner side of the bend at each z^* were 0, 45, 90, 135 and 180º. The liquid film thicknesses on the top and bottom sides in the horizontal section were also measured. At $z^* = 4$, the base film at θ = 0º was thicker than that at the other θ in most of the present experimental conditions. In contrast, the circumferential distribution of the base film thickness was symmetric even at $z^* = 4$ in the cases of high gas volumetric flux and low liquid volumetric flux. The circumferential distributions of the base film thicknesses at $z^* = 12$ and 20 were symmetric in all experimental conditions. At $z^* = 12$ and 20, the circumferential averaged base film thickness after passing through the bend with $R^* = 10$ was larger than that after passing through the bend with $R^* = 6$. The axial velocity in the liquid film was also measured. The circumferential distribution of the axial velocity was nearly symmetric at $z^* = 12$ and 20.

Keywords: Upward annular flow; Liquid film thickness; 90º bend; Laser-induced fluorescence; Liquid film velocity

1. Introduction

Distribution of gas-liquid two-phase flows from an upstream pipe to multiple downstream pipes is one of important technical topics in industrial devices such as heat exchanges, oil and chemical plants. For heat exchangers, devices such as branch junctions and distributors are utilized for distribution of refrigerant two-phase flows. Several studies on gas-liquid two-phase flows through a distributor have been carried out, since the energy efficiency of heat exchangers depends on its distribution performance (Asano et al., 1999; Yoshioka et al., 2008; Wu et al., 2019). An upstream pipe connected to the distribution devices often has a bend, which implies the centrifugal force causes a non-axisymmetric cross-sectional distribution of gas and liquid phases. Actually, Yoshimura and Ishii (2012) showed that distribution ratio of gas and liquid phases at the outlets of a T-junction after passing through a U-bend is affected by a non-axisymmetric phase distribution due to the presence of the bend. Annular flow is a typical flow pattern in pipes of heat exchangers. It is therefore required to obtain knowledge on the circumferential distribution of the liquid film thickness of annular flows after passing through a bend for high energy efficiency of heat exchangers.

There are several studies on axial development of an upward annular flow in a vertical pipe. Wolf et al. (2001) reported that the liquid film thicknesses of upward annular flows in a vertical pipe with pipe diameter D of 31.8 mm increase with increasing the dimensionless axial distance z^* for $z^* \leq 8$ and then decrease with increasing z^*, where z^* is the ratio of the axial distance z to D. The annular flows required 100 to 300 times as long as the pipe diameter to reach developed flows. Hazuku et al. (2008) measured the liquid film thickness of upward annular flows in a vertical pipe of $D = 11$ mm for $50 \leq z^* \leq 250$ and the measured liquid film thickness decreased with increasing z^*. Waltrich et al. (2013) reported that the liquid volume fraction of upward annular flows in a vertical pipe of $D = 48$ mm for $102 \leq z^* \leq 815$ decreases with increasing z^*. Axial development of non-axisymmetric phase distributions due to the presence of a bend, however, has not been reported, i.e. there is no knowledge on the transition from a non-axisymmetric distribution to an axisymmetric distribution.

A change from a horizontal flow to an upward flow appears at a 90º bend in piping systems. There are, however, a few studies on upward flows in a vertical section after flowing in a horizontal section (Legius, 1997; Saidj et al., 2014). These studies dealt with bubbly, slug and churn flows in large diameter pipes for $D \geq 34$ mm, that is, there are no

studies on upward annular flows after passing through a 90º bend in small diameter pipes. The axial velocity of a single phase pipe flow after passing through a 90° bend takes a peak near the outer side wall, while the axial velocity near the inner side wall is low due to flow separation (Sudo et al., 1998; Röhrig et al., 2015). The relation between the liquid film thickness and the axial velocity should be understood to consider liquid distribution at distribution devices.

The liquid film thicknesses of upward air-water annular flows after passing through a 90º bend, therefore, were measured by means of the planer laser-induced fluorescence (Schubring et al., 2010) in the present study. The measurements were at five circumferential positions from 0º to 180º with an interval of 45º and at three elevations in the vertical section to discuss axial development of the base film thickness with respect to the distance from the bend. We also measured the liquid film thicknesses on the top and bottom sides in the horizontal section, i.e. boundary condition at the inlet of the bend. Axial velocities of the liquid film at representative measurement positions were measured by means of the particle tracking velocimetry.

2. Experimental method

Figure 1 shows the experimental setup, which consists of the air and water supply systems, the lower and upper tanks, the gas-liquid mixture section, the flow channel consisting of the horizontal section, the 90º bend and the vertical section. The channel was cylindrical, i.e. pipe, and its diameter D was 5.0 mm. The ratios, R^* (= R/D), were 6 and 10, where R is the radius of curvature of the bend. The horizontal and vertical sections and the bend were made of transparent acrylic resin. Tap water and air were used as the liquid and gas phases, respectively. The pump (Iwaki, MD-30R-N) supplied water in the lower tank to the mixing section and its flow rate was measured by the flow meter (Nippon flow cell, NSP-6). The compressor (Anest iwata, OFP-071C) was used for the air supply and the flow meter (Nippon flow cell, NSP-6) measured the flow rate of air. Mixed air and water at the mixing section flowed through the horizontal section, the bend and the vertical section. Air and water were discharged into atmosphere in the upper tank. The temperature of water were 298 $\pm$ 2K. The gas volumetric flux, J_G, ranged from 5 to 20 m/s and the liquid volumetric flux, J_L, was 0.5 and 0.9 m/s. Uncertainties estimated at 95% confidence level in the measured gas and liquid flow rates were ±1.9 and ±1.2%, respectively.

Figure 2 shows the schematic of the flow channel and the measurement positions. The symbols O_x and O_z mean the ends of the bend connected to the horizontal section and the vertical section, respectively. The dimensionless distance, x^* (= x/D), of the measurement position in the horizontal section was 20, where x is the distance from O_x. The

dimensionless distances, z^* (= z/D), of the measurement positions in the vertical section were 4, 12 and 20, where z is the distance from O_z. The circumferential coordinate θ was defined from the outer side of the bend to the inner side of the bend, i.e. from 0° to 180°. The circumferential coordinates of measurement positions were 0, 45, 90, 135 and 180°.

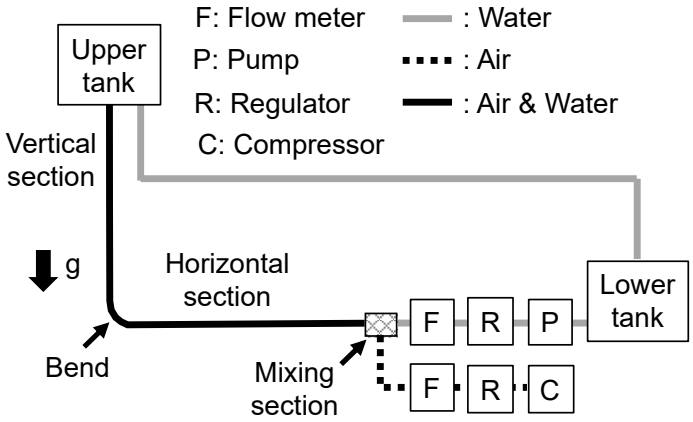

Fig. 1 Experimental setup

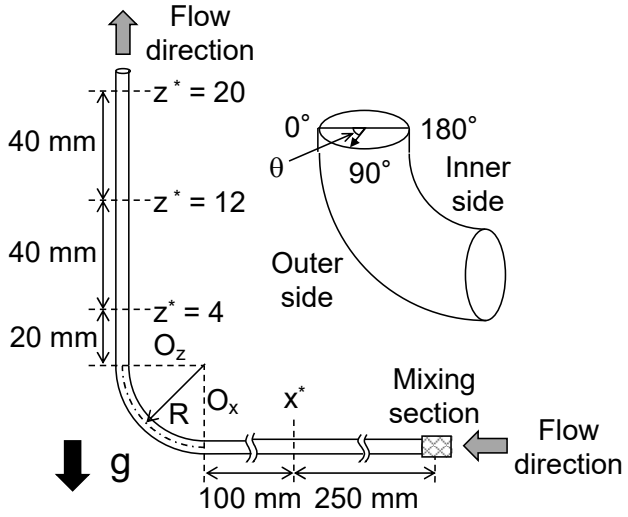

Fig. 2 Channel geometry and measurement position

The liquid film thickness was measured by means of the planer laser-induced fluorescence (PLIF) (Schubring et al., 2010). For the measurement, Rhodamine B (Hayashi Pure Chemical Ind., Ltd.) was mixed into tap water. Images were recorded by using the high-speed video camera (Photron, FASTCAM Mini UX50; flame rate = 500 frames/s, exposure time = 10 μs, spatial resolution ≃ 0.0043 mm/pix). The laser with the wave length

of 532 nm (Civillaser, LSR532H) was used for illumination. Figure 3 shows the layout of the vertical pipe and the measurement instruments. The pipe was covered by the octagonal jacket made of transparent acrylic resin. Each edge length of the jacket was larger than the inner pipe diameter, so that we obtain images in the diagonal (45 and 135°) and perpendicular (90°) planes to the basic (0 and 180°) plane. Since the laser beam decays due to fluorescence in the liquid film and reflects at the gas-liquid interface, available images for the measurement of the liquid film at θ = 180° were not obtained simultaneously in the measurements at θ = 0°, i.e. images at each position were recorded separately as shown in Fig. 3. A red optical filter was installed on the camera lens to cut scattered light at the interfaces of gas-liquid and liquid-wall. Measurement values of the liquid film thicknesses were obtained by applying image processing to obtained images. Figure 4(a) shows an example of an original image including the gas-liquid interface. The gray and black regions represent water and gas, respectively. The image was trimmed at the pipe wall in the horizontal direction and for 30 pixels in the vertical direction. The sigmoid function was applied to images for contrast enhancement (Fig. 4(b)). The sharpened image was obtained by applying the laplacian filter (Fig. 4(c)). Noise in the image was removed by applying the Median filter (Fig. 4(d)). The binarized image was obtained (Fig. 4(e)). The distance, d_i, between the left side wall and the right boundary of the white region at each elevation in the image was calculated. Optical distortion due to the curved surface of the inner pipe wall was corrected based on the Snell's law. We derived a relation between a radial distance in an image and an actual radial distance, i.e. without optical distortion. An additional distance calculated from the relation was considered in the calculation of d_i. We checked the relation by measuring a stainless steel ball with 4.75 mm diameter installed in the pipe and the measured diameter with an additional distance agreed well with the actual diameter of the ball within 1.9% error. Images in which large amplitude waves such as disturbance waves appear were neglected since d_i of the waves cannot be measured due to the difficulty of detection of the interface. Thus, the obtained film thicknesses were regarded as the base film of an annular flow (Fukano and Ousaka, 1989). The base film thickness, t_j, in an image was calculated by

$$t_j = \frac{1}{N}\sum_{i=1}^{N} d_i \tag{1}$$

where N is the number of pixels in the vertical direction, i.e. 30 pixels. The base film thickness, t, in each case was calculated by

$$t = \frac{1}{M}\sum_{j=1}^{M} t_j \tag{2}$$

where M is the number of images. The M was more than 3500 in each case. Uncertainty estimated at 95% confidence level in t was less than 1.8%.

We measured the surface tension between air and tap water with and without Rhodamine B using the pendant bubble method (Pan et al., 1998). The measured surface tension without Rhodamine B was 72.0 mN/m. The surface tension was measured at three types of concentration of Rhodamine B, 0.005, 0.01 and 0.015 g/L, and the measured values of the surface tension were 71.9, 71.0 and 68.0 mN/m, respectively. Hence, the surface tension decreased with increasing the concentration of Rhodamine B. Based on the measurement results, we determined the concentration of Rhodamine B in the measurement of the liquid film thickness as 0.005 g/L, since the surface tension at the concentration is nearly equal to that without Rhodamine B.

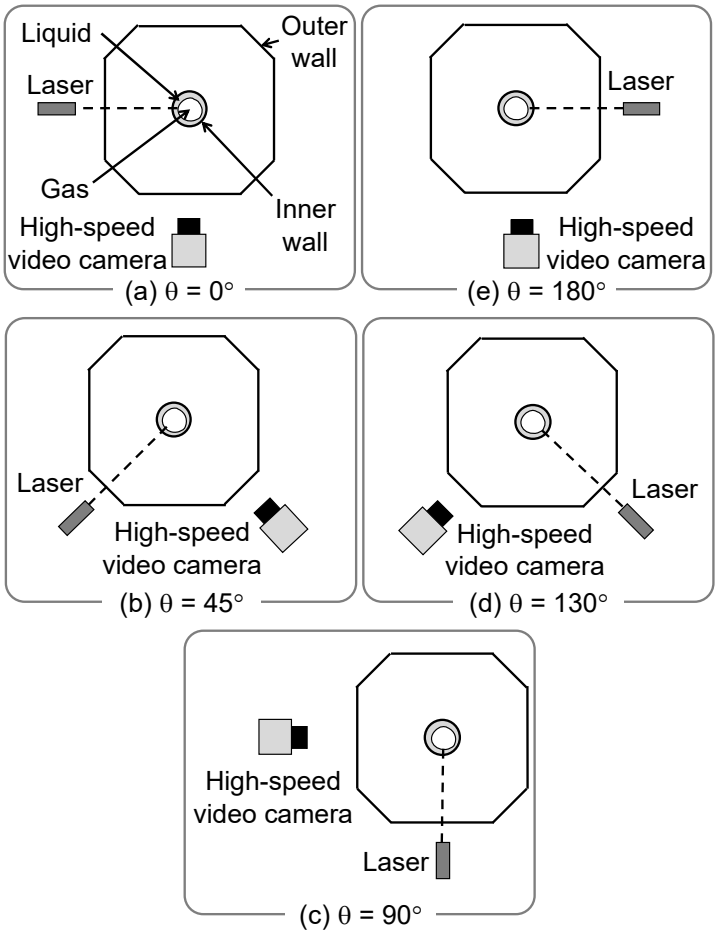

Fig. 3 Measurement layout for liquid film thickness

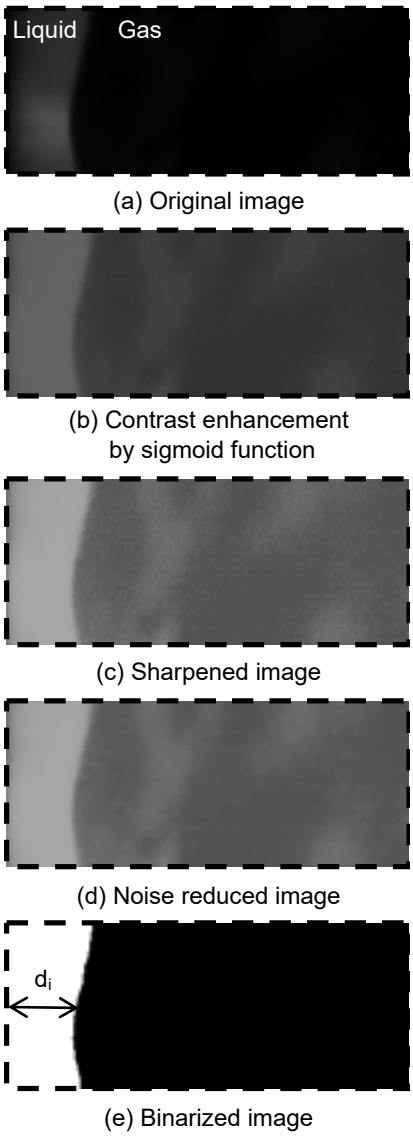

Fig. 4 Image processing procedure for measurement of liquid film thickness

The axial velocity V_z in the liquid film was measured by applying the particle tracking velocimetry (PTV) to images recorded by the high-speed video camera (Photron, FASTCAM Mini UX50; flame rate = 10000 frames/s, exposure time = 10 μs, spatial resolution $\simeq$ 0.0043 mm/pix) with the LED back light. Silicon carbide (SiC) particles with average diameter of 15 μm were mixed in tap water as seeding particles, since we have confirmed that the SiC particles in low concentrations do not affect motion of the gas-liquid interface (Kurimoto et al. 2016). The concentration of the particles was less than 0.3 wt%. The measurement layout is shown in Fig. 5. This measurement gives line-averaged values of V_z in the radial direction in the liquid film at a measurement position, whereas large

deviation caused by the radial position of a seeding particle is expected in principle. We calculated velocities of visible particles at the central part in two successive images and those averaged-values were based on 60 data with at least 0.25s intervals. The average of uncertainty estimated at 95% confidence level in V_z was 15%.

In addition, flows in the horizontal and vertical sections were observed by using the high-speed camera. Time-strip flow visualization technique (Borhani et al., 2010; Goda et al., 2021) was applied to the obtained images to understand the flow characteristics. Figure 6 shows an example of the time-strip flow visualization technique. The gray values of the middle row perpendicular to the axial direction were extracted from each image and rearranged in the vertical direction, i.e. the vertical axis of the time-strip image represents the time *t*.

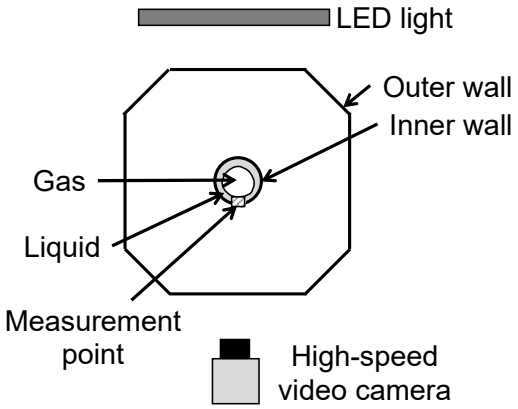

Fig. 5 Measurement layout for particle tracking velocimetry

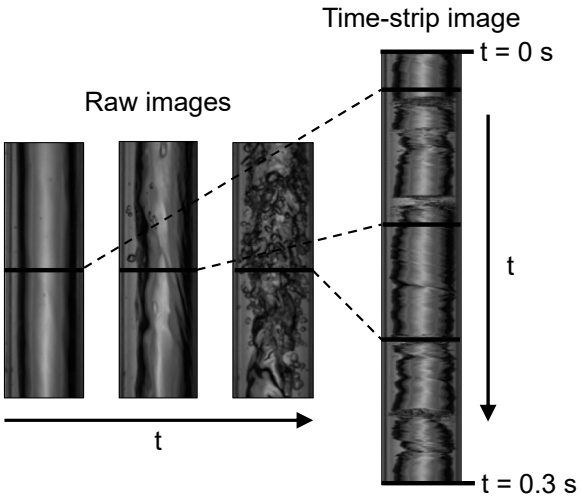

Fig. 6 Time-strip visualization technique

3. Results and discussion

Time-strip images at low and high J_G in the horizontal section are shown in Figs. 7(a) and (b), respectively. The horizontal section in the images was connected with the bend of $R^* = 6$. The flow pattern in Fig. 7(a) is similar to annular flow, i.e. the annular liquid film forms along the pipe wall and the gas flows in the center of the pipe. However, large wavy deformations of the gas-liquid interface occur as represented by the white broken lines. Coleman and Garimella (1999) observed such the flow pattern, referred to as wavy-annular flow, in horizontal pipes with small diameters from 1.3 to 5.5 mm. The liquid film thickness on the top side of the pipe is smaller than that on the bottom side of the pipe due to the gravitational force. The flow pattern in Fig. 7(b) is annular flow. The black streaks perpendicular to the axial direction indicate disturbance waves. The liquid film thickness is smaller than that at $J_G = 5$ m/s and the difference in the liquid film thicknesses between the top and bottom is slight.

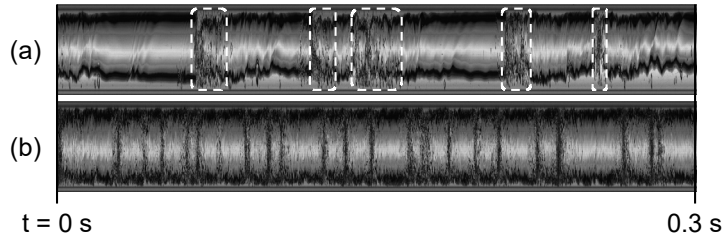

Fig. 7 Time-strip images in horizontal section at $J_L = 0.5$ m/s
((a) $J_G = 5$ m/s, (b) $J_G = 20$ m/s)

Figure 8 shows the base film thickness on the top side, t_t, and that on the bottom side, t_b, in the horizontal section scaled by the pipe diameter. The data shown in the figure are in the horizontal section with the bend of $R^* = 6$ downstream since we experimentally confirmed the effect of R^* on the base film thickness in the horizontal section is negligible. The Froude number, Fr, is defined by

$$Fr = \frac{J_G}{\sqrt{(\rho_L - \rho_G) g D / \rho_G}} \tag{3}$$

where ρ is the density, g the gravity of acceleration and the subscript G and L denote the gas and liquid phases, respectively. The base film thicknesses on both sides decrease with increasing Fr. The base film thickness on the top side is much smaller than that on the bottom side at low Fr. In contrast, the difference in the thicknesses between both sides

disappears at high *Fr*.

Figure 9 shows the ratio, t_t/t_b, of the base film thickness on the top side to that on the bottom side. The cross symbols represent experimental data of air-water annular flows obtained by Luninski et al. (1983) and the solid line represents the following correlation proposed by Cioncolini and Thome (2013):

$$\frac{t_t}{t_b} = \frac{0.0789Fr^{1.90}}{1 + 0.0789Fr^{1.90}} \qquad (Fr > 1) \tag{4}$$

The measured t_t/t_b increases with *Fr*, which is consistent with the data of Luninski et al. and the correlation. The increase in t_t/t_b is caused by the large decrease in t_b shown in Fig. 8. The data of Luninski et al. and the correlation, however, are lower than the present experimental data. The difference in *D* would be main cause of the difference in t_t/t_b. Donniacuo et al. (2015) and Layssac et al. (2017) pointed out that the liquid film thicknesses on the top and bottom sides approaches symmetric with decreasing the Eötvös number, *Eo* (= $(\rho_L - \rho_G)gD^2/\sigma$), which is the ratio of the buoyant force to the surface tension force. The data of Luninski et al. are for $D \geq 8.15$ mm and *Eo* at $D = 8.15$ mm is 2.7 times as large as that at $D = 5.0$ mm. The correlation is much lower since based on data for $8.15 \leq D \leq 95.3$ mm. The measured t_t/t_b at $Fr = 3.0$ is almost unity, i.e. the circumferential distribution of the base film thickness would be regarded as symmetric. Dependence of t_t/t_b on J_L is weak in the present experimental range.

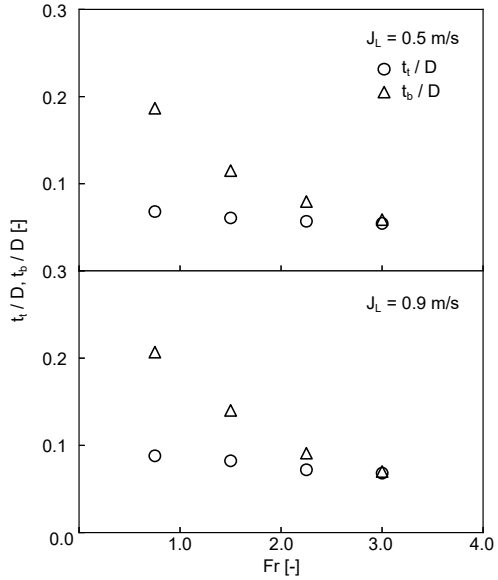

Fig. 8 Base film thickness on top and bottom sides in horizontal section

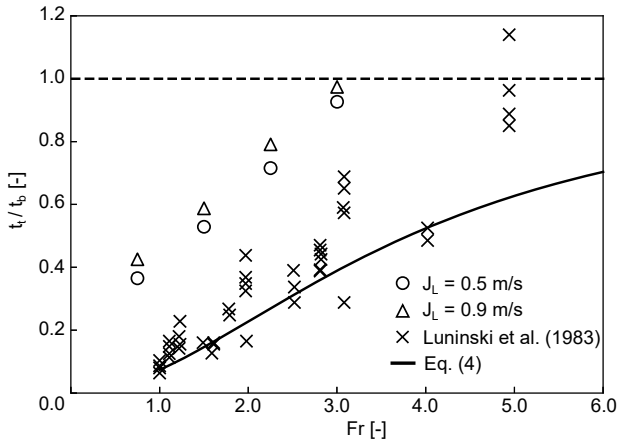

Fig. 9 Comparison of t_t/t_b with experimental data and correlation

Figure 10 shows time-strip images of upward flows after passing through the bend with $R^* = 6$. At $J_G = 5$ m/s, the large wavy deformation observed in the horizontal section remains in the vertical section. The difference in the liquid film thicknesses between the left and right sides in the vertical section becomes smaller with increasing z^* at $J_G = 5$ m/s. The liquid film thicknesses between the left and right sides at $J_G = 20$ m/s are almost the same even at $z^* = 4$.

Fig. 10 Time-strip images of upward flows after passing through bend
with $R^* = 6$ at $J_L = 0.5$ m/s
((i-a) $z^* = 4$, $J_G = 5$ m/s; (i-b) $z^* = 4$, $J_G = 20$ m/s;
(ii-a) $z^* = 20$, $J_G = 5$ m/s; (ii-b) $z^* = 20$, $J_G = 20$ m/s)

Figure 11 shows the circumferential distribution of the base film thickness, t, in the vertical section in r-θ coordinates, where r is the radial coordinate. The ratio R^* is 6. The base film at θ = 0° is thicker than that at the other θ at $z^* = 4$ in Fig. 11(i-a). With increasing z^*, t at θ = 0 and 45° decrease and the variation of t at the other θ is slight. The circumferential distribution of t at z^* =12 and 20 results in nearly symmetric. Although the thick liquid films at θ = 0° and $z^* = 4$ are also observed in Figs. 11 (i-b) and (i-c), the difference in t between θ = 0° and the other θ decreases with increasing J_G. At the highest J_G (Fig. 11 (i-d)), t at θ = 0° and $z^* = 4$ is nearly equal to that at the other θ, i.e. the circumferential distribution of t is symmetric even immediately after passing through the bend. Dependence of t at $z^* = 4$ on J_G can be understood from the data in the horizontal section. As shown in Fig. 9, t_t/t_b increases with increasing Fr and reaches nearly unity at Fr = 3.0, i.e. J_G = 20 m/s. At low J_G, the thick liquid film on the bottom side in the horizontal section due to the gravitational force remains at $z^* = 4$. The thin liquid film at high J_G also remains after passing through the bend without remarkable effects of the centrifugal force. The distribution of the liquid film thickness in the horizontal section, therefore, relates to that in the vertical section. The tendency of t on J_G at J_L = 0.9 m/s is consistent with that at J_L = 0.5 m/s as shown in Fig. 11(ii).

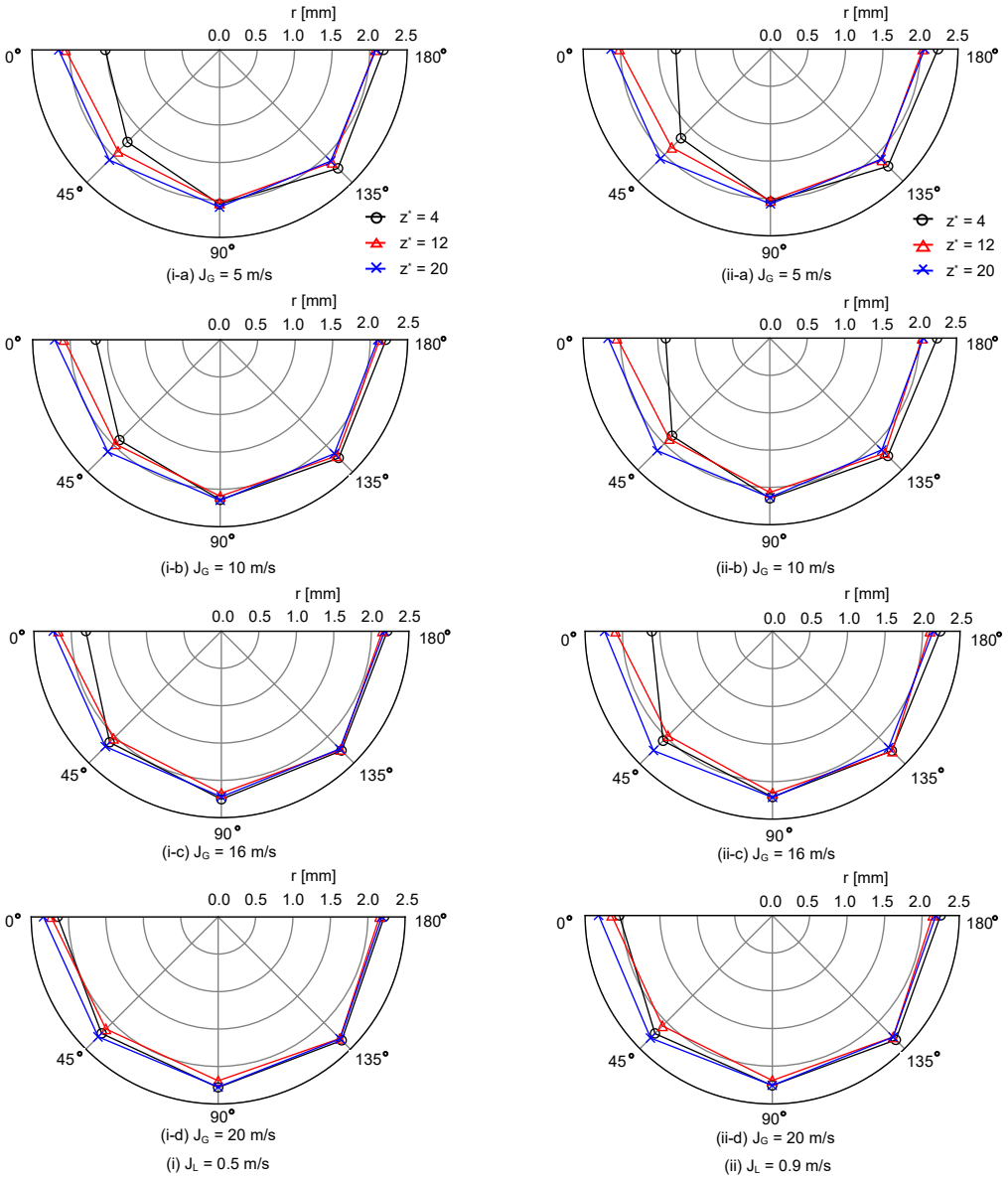

Fig. 11 Circumferential distribution of base film thickness in vertical section ($R^* = 6$)

Figure 12 shows the circumferential distribution of t in the vertical section at $R^* = 10$. At low J_G, the base film at θ = 0° and $z^* = 4$ is thicker than that at the other θ. Compared with the data in Fig. 11, the base film at θ = 0° and $z^* = 4$, however, is thinner. The base film at θ = 180° and $z^* = 4$ is remarkably thinner than that at the other θ. Thus, the increase in R^* causes the decrease in t at both θ = 0 and 180°. The circumferential distribution of t approaches a symmetric distribution with increasing z^*. At the highest J_G, the circumferential distribution of t even at $z^* = 4$ is nearly symmetric.

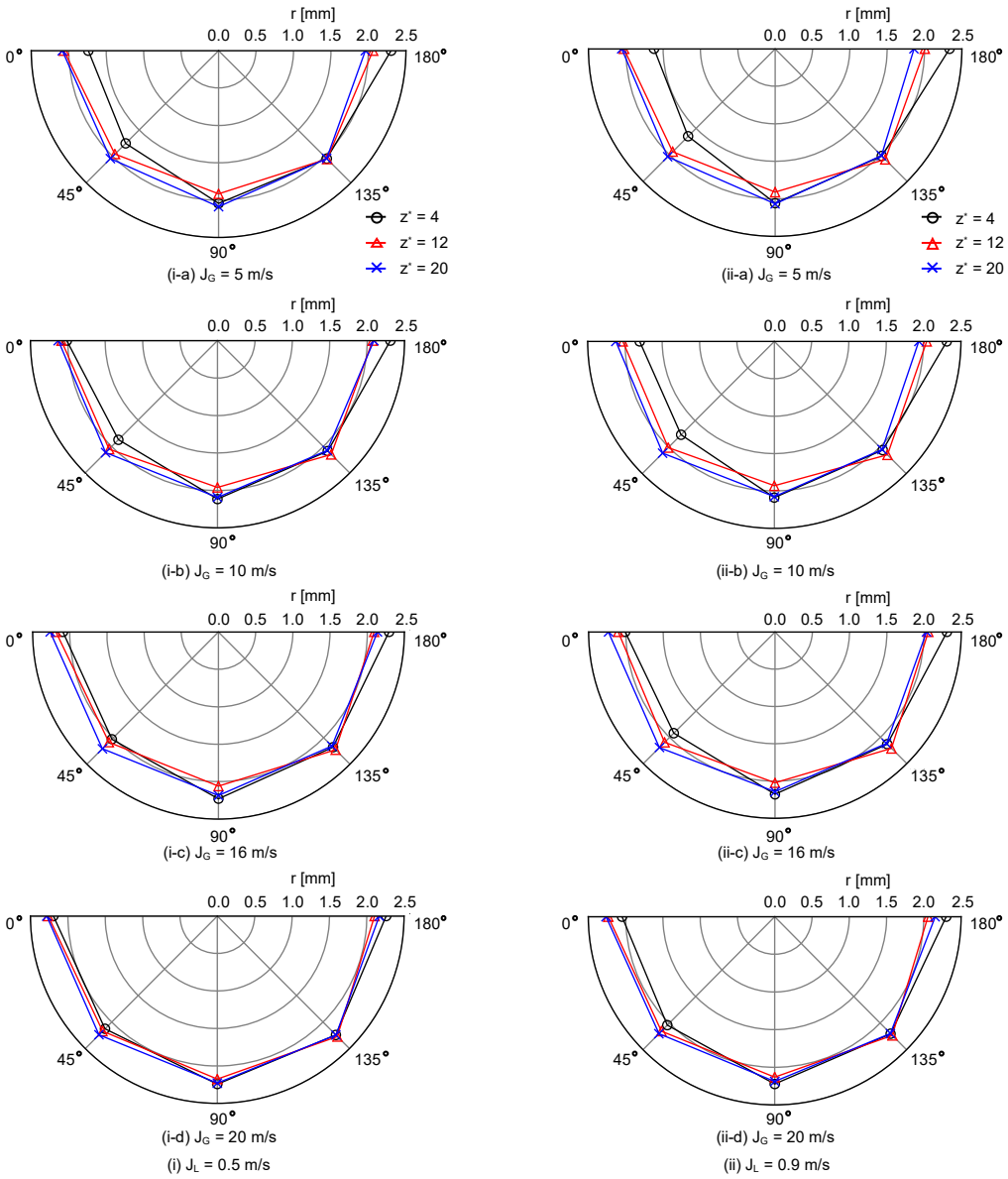

Fig. 12 Circumferential distribution of base film thickness in vertical section ($R^* = 10$)

Figures 13(a) and (b) show dependences of the thickness ratios $t_{180°}/t_t$ and $t_{0°}/t_b$ on Fr, respectively, where $t_{180°}/t_t$ is the ratio of t at $\theta = 180^\circ$ and $z^* = 4$ to t_t and $t_{0°}/t_b$ is the ratio of t at $\theta = 0^\circ$ and $z^* = 4$ to t_b. Most of $t_{180°}/t_t$ are less than unity. This result indicates that liquid moves to the outer side of the bend due to the centrifugal force when passing through the bend. The thickness ratio $t_{180°}/t_t$ at $R^* = 6$, however, is larger than that at $R^* = 10$ in spite of the larger centrifugal force. This might be caused by a secondary flow in the liquid film. As shown in Appendix A, we observed motion of particles in the liquid film passing through the bend. Some particles in the bend with $R^* = 6$ move to the inner side in the upper half of the bend, whereas particles taking such trajectory are not observed in the bend with $R^* = 10$. The liquid on the top in the horizontal section moves to the outer side in the lower half of the bend and then part of the liquid might return to the inner side in the upper half of the bend with $R^* = 6$. The thickness ratio $t_{0°}/t_b$ at $R^* = 6$ is larger than unity, whereas most of $t_{0°}/t_b$ at $R^* = 10$ is nearly equal to unity. This would be caused by the magnitude of the centrifugal force. The radical decrease in $t_{0°}/t_b$ for $Fr \geq 2.3$ at $R^* = 6$ is caused by a parabolic decrease in $t_{0°}$ and an asymptotic decrease in t_b with respect to Fr.

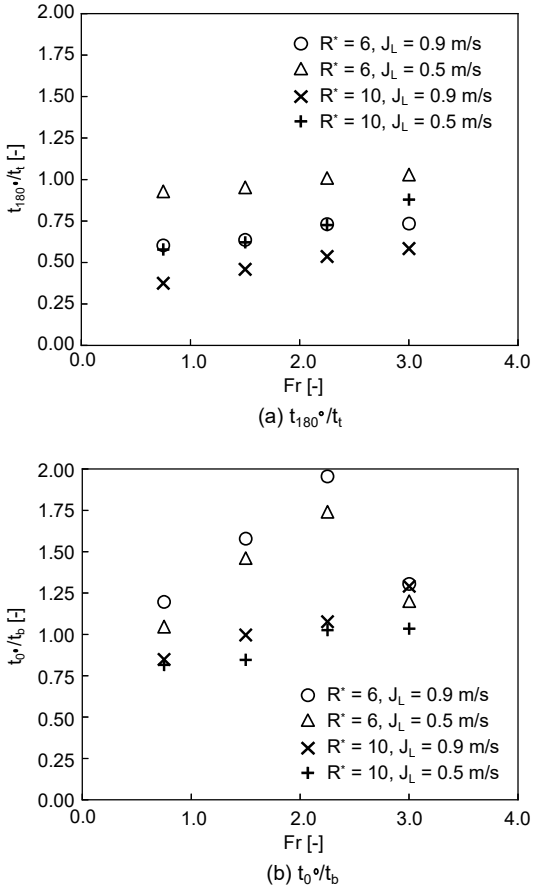

Fig. 13 Thickness ratios $t_{180°}/t_t$ and $t_{0°}/t_b$

Figure 14 shows the base film thickness t with standard deviation represented as error bars to make the relation between t and fluctuation of the gas-liquid interface clear. At low J_G, the standard deviations at $z^* = 4$ are large at θ = 0 and 45° due to the large t. The large standard deviation decays with increasing z^*, which results in nearly uniform standard deviation with respect to θ. At high J_G, the circumferential distribution of the standard deviation is nearly uniform even at $z^* = 4$ since that of t is symmetric.

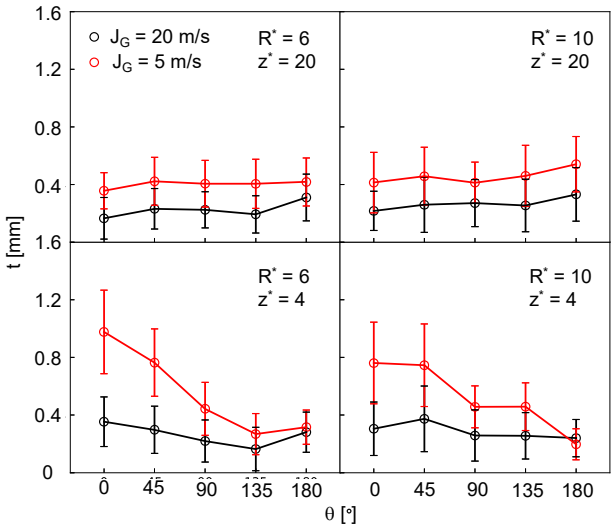

Fig. 14 Base film thickness with standard deviation

The relation between the dimensionless circumferential averaged base film thickness, $\bar{t}/D$, and Fr is shown in Fig. 15, where $\bar{t}$ is the average of t from 0° to 180° at each z^*. The $\bar{t}/D$ decreases with increasing Fr as reported by previous studies on the liquid film thickness of upward annular flows in vertical pipes (e.g. Fukano and Furukawa, 1998). The $\bar{t}/D$ decreases with increasing z^* as reported by Wolf et al. (2001) and Hazuku et al. (2008). The $\bar{t}/D$ after passing through the bend with $R^* = 10$ is larger than that after passing through the bend with $R^* = 6$ except for the data at $z^* = 4$, i.e. the bend ratio affects the base film thickness in the vertical section. This result might relate to the frequency of large amplitude waves such as large wavy deformation and disturbance waves shown in Fig. 10. We confirmed that the frequencies of the large amplitude waves observed at $z^* = 20$ increase by at most 1.3 times due to the decrease in R^*. Thus, the amount of liquid transferred by the waves would be large at $R^* = 6$, which results in the thinner base film.

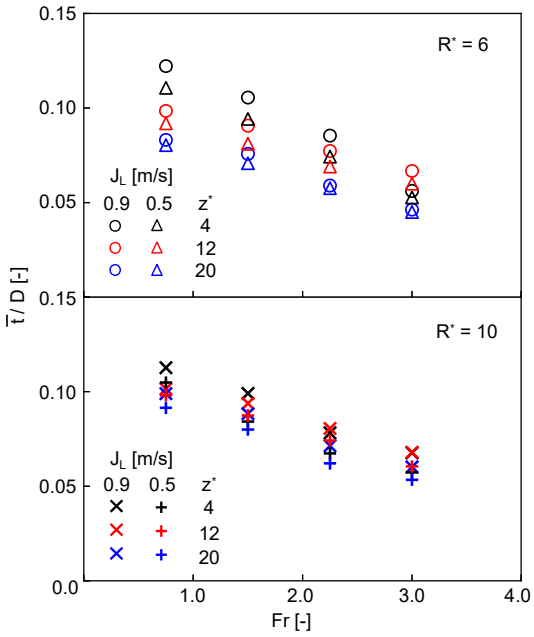

Fig. 15 Dimensionless circumferential averaged base film thickness

Figure 16 shows the coefficient of variation, *CV*, against *Fr*. The *CV* is defined by

$$CV = \frac{\sigma_t}{\bar{t}} \tag{5}$$

where σ_t is the standard deviation of *t*. The coefficient of variation is regarded as an indicator evaluating the symmetricity of *t*. Most of *CV* at $z^* = 4$ are large due to the thick liquid film at $\theta = 0^\circ$ as shown in Figs. 11 and 12. The coefficient of variation at $z^* = 12$ and 20 are small regardless of J_L and *Fr*, i.e. the circumferential distributions of *t* are symmetric. In the case of the highest *Fr* and low J_L, the coefficient of variation is the same level as that at $z^* = 12$ and 20, i.e. the circumferential distribution of *t* is regarded as symmetric even at $z^* = 4$.

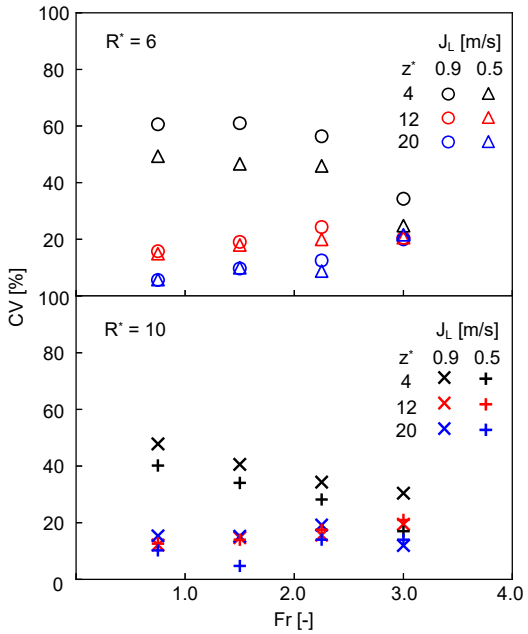

Fig. 16 Coefficient of variation *CV* of circumferential averaged base film thickness

Figure 17 shows the axial velocity V_z in the liquid film in the vertical section. The error bars represent 95 % confidence level in V_z. At $z^* = 4$, the axial velocity at $\theta = 0^\circ$ is the largest and that at $\theta = 180^\circ$ is the smallest. It is well-known that the axial velocity of a single phase flow in a straight pipe after passing through a 90° bend takes a peak near the outer side, while the axial velocity near the inner side is low due to flow separation (Sudo et al., 1998; Röhrig et al., 2015). The axial velocity V_z at the inner side is remarkably low at low J_G. This would be caused by weak interfacial shear stress at the inner side. Effects of R^* on the difference in V_z is slight. The differences in V_z among the circumferential measurement positions are small at $z^* = 12$ and 20, i.e. the circumferential distribution of V_z is nearly symmetric.

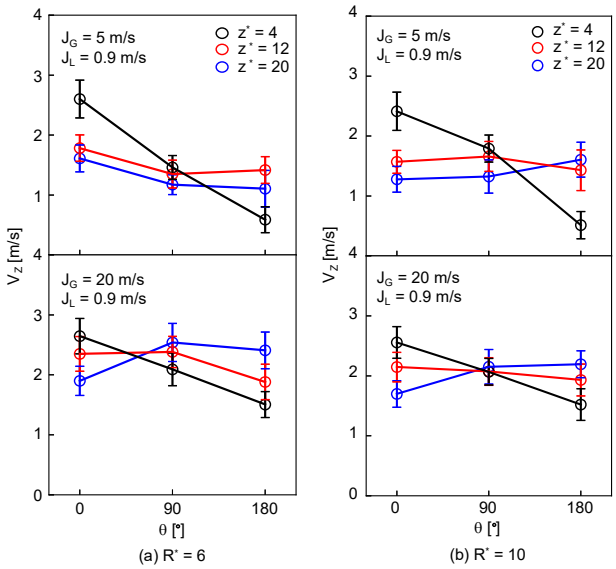

Fig. 17 Axial velocity V_z in the liquid film in vertical section

4. Conclusion

The liquid film thickness of air-water annular flows in horizontal and vertical pipes connected by a 90º bend was measured by means of the planer laser laser-induced fluorescence. The pipe diameter D was 5.0 mm and the ratios, R^*, of the radius of curvature of the bend to D were 6 and 10. The base film thicknesses on the top and bottom sides, t_t and t_b, in the horizontal section were measured at x^* (= x/D) = 20, where x is the horizontal distance from the end of the bend. The measurement positions in the vertical section located at z^* (= z/D) = 4, 12 and 20 and θ = 0, 45, 90, 135 and 180º, where z is the vertical coordinate from the end of the bend and θ is the circumferential coordinate from the outer side of the bend to the inner side of the bend. The axial velocities in the liquid film were measured in the vertical section by means of the particle tracking velocimetry to confirm effects of the change in the flow direction. The following conclusions were obtained:

(1) The base film at θ = 0º and z^* = 4 is thicker than that at the other θ in most of the present experimental conditions. In contrast, the circumferential distribution of the base film thickness in the vertical section is symmetric even at z^* = 4 in the cases of high J_G and low J_L since t_t/t_b is nearly unity in the horizontal section.

(2) The circumferential distribution of the base film thickness at z^* = 12 and 20 is symmetric in the present experimental conditions.

(3) At z^* = 12 and 20, the circumferential averaged base film thickness after passing through the bend with R^* = 10 is larger than that after passing through the bend with R^* = 6. This might relate to the frequency of large amplitude waves.

(4) The circumferential distribution of the axial velocity in the liquid film is nearly symmetric at $z^* = 12$ and 20, whereas the axial velocities at $z^* = 4$ are large and small at $\theta = 0^o$ and 180^o, respectively.

Acknowledgement

The authors would like to express their gratitude to Mr. Shun Miyawaki and Mr. Ryo Okamoto for their assistance in experiments. This work has been supported by MAYEKAWA HOUONKAI FOUNDATION.

Appendix A. Particle motion in bend with $R^* = 6$

We observed motion of SiC particles passing through the bend. An example of particle motion in the bend with $R^* = 6$ is shown in Fig. A1. The red circles in the figures indicate the positions of the particle at each time. The particle observed in Fig. A1(b) passes through an invisible region due to reduction in transmission caused by curvature of the gas-liquid interface for $1.5 \times 10^{-3} < t < 6.0 \times 10^{-3}$ s. We presume that the particles in Figs. A1(b) and (c) are likely the same accounting for its trajectory and weak particle concentration. The particle moves to the outer side of the bend for $t \leq 1.5 \times 10^{-3}$ s due to the centrifugal force. In contrast, the particle for $t \geq 6.0 \times 10^{-3}$ s moves to the inner side of the bend. Thus, part of the liquid along the outer side flows toward the inner side in the upper half of the bend. Some particles take such trajectory in $R^* = 6$, whereas particles passing through the bend with $R^* = 10$ keep moving along the curved channel, i.e. the secondary flow toward the inner side is weak.

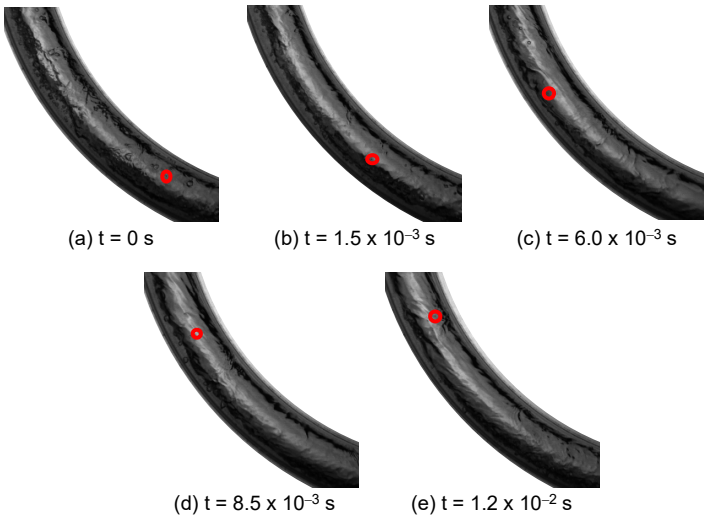

Fig. A1 Particle motion in bend with $R^* = 6$
($J_G = 16$ m/s, $J_L = 0.9$ m/s)

Reference

Asano, H., Takenaka, N., Fujii, T., Shibata, Y., Ebisu, T., and Matsubayashi, M., 1999. Visualization and measurement of refrigerant flow in compression-type refrigerator by neutron radiography, Nuclear Instruments and Methods in Physics Research Section A: Accelerators, Spectrometers, Detectors and Associated Equipment, 424, 98–103.

Borhani, N., Agostini, B., and Thome, J.R., 2010. A novel time strip flow visualisation technique for investigation of intermittent dewetting and dryout in elongated bubble flow in a microchannel evaporator, International Journal of Heat and Mass Transfer, 53, 4809–4818.

Cioncolini, A., and Thome, J.R., 2013. Liquid film circumferential asymmetry prediction in horizontal annular two-phase flow, International Journal of Multiphase Flow, 51, 44–54.

Coleman, J.W., and Garimella, S., 1999. Characterization of two-phase flow patterns in small diameter roud and rectangular tubes, International Journal of Heat and Mass Transfer, 42, 2869-2881.

Donniacuo, A., Chrnay, R., Mastrullo, R., Mauro, A. W., and Revellin, R., 2015. Film thickness measurements for annular flow in minichannels: Description of the optical technique and experimental results, Experimental Thermal and Fluid Science, 69, 73-85.

Fukano, T., and Ousaka, A., 1989. Prediction of the circumferential distribution of film thickness in horizontal and near-horizontal gas-liquid annular flows, International Journal of Multiphase Flow, 15(3), 403-419.

Fukano, T., and Furukawa, T., 1998. Prediction of the effects of liquid viscosity on interfacial shear stress and frictional pressure drop in vertical upward gas-liquid annular flow, International Journal of Multiphase Flow, 24, 587–603.

Goda, R., Kurimoto, R., Hayashi, K., Murase, M., and Tomiyama, A., 2021. Effects of fluid properties on interfacial and wall friction factors under counter-current flow limitation in a vertical pipe with sharp-edged lower end, Nuclear Engineering and Design, 373, 111020.

Kurimoto, R., Yasuda, T., and Minagawa, H., 2016. Effects of surfactant on quasi-static bubble growth from an orifice, Chemical Engineering and Processing: Process Intensification, 104, 154-159.

Layssac, T., Capo, C., Lips, S., Mauro, A. W., and Revellin, R., 2017. Prediction of symmetry during intermittent and annular horizontal two-phase flows, International Journal of Multiphase Flow, 95, 91–100.

Legius, H.J.W.M., 1997. Propagation of pulsations and waves in two-phase pipe systems, Delft University of Technology.

Luninski, Y., Barnea, D., and Taitel, Y., 1983. Film thickness in horizontal annular flow, The Canadian Journal of Chemical Engineering, 61, 621–626.

Hazuku, T., Takamasa, T., and Matsumoto, Y., 2008. Experimental study on axial development of liquid film in vertical upward annular two-phase flow, International Journal of Multiphase Flow, 34, 111–127.

Pan, R., Green, J., and Maldarelli, C., 1998. Theory and experiment on the measurement of kinetic rate constants for surfactant exchange at an air/water interface, Journal of Colloid and Interface Science, 205, 213–230.

Röhrig, R., Jakirlic, S., and Tropea, C., 2015. Comparative computational study of turbulent flow in a 90° pipe elbow, International Journal of Heat and Fluid Flow, 55, 120-131.

Saidj, F., Kibboua, R., Azzi, A., Ababou, N., and Azzopardi, B.J., 2014. Experimental investigation of air-water two-phase flow through vertical 90° bend, Experimental Thermal and Fluid Science, 57, 226–234.

Schubring, D., Ashwood, A.C., Shedd, T.A., and Hurlburt, E.T., 2010. Planar laser-induced fluorescence (PLIF) measurements of liquid film thickness in annular flow. Part I: Methods and data, Internationl Journal Multiphase Flow, 36, 815–824.

Sudo, K., Sumida, M., and Hibara, H., 1998. Experimental investigation on turbulent flow in a circular-sectioned 90-degree bend, Experiments in Fluids, 25, 42-49.

Yoshimura, K., and Ishii, E., 2012. Distribution Prediction for Distributor using Gas-liquid Flow Simulation with Liquid Film Modification, Transaction of the Japan Society of Refrigerating and Air Conditioning Engineers, 29, 331–342, (in Japanese).

Yoshioka, S., Kim, H., and Kasai, K., 2008. Performance Evaluation and Optimization of A Refrigerant Distributor for Air Conditioner, Journal of Thermal Science and Technology, 3, 68–77.

Waltrich, P., Falcone, G., and Barbosa Jr., J. R., 2013. Axial development of annular, churn and slug flows in a long vertical tube, International Journal of Multiphase Flow, 57, 38-48.

Wolf, A., Jayanti, S., and Hewitt, G. F., 2001. Flow development in vertical annular flow, Chemical Engineering Science, 56, 3221-3235.

Wu, G., Ren, T., Ding, G., and Yu, B., 2019. Design and visualized validation of a distributor with uniform refrigerant distribution by forming annular flow, International Journal of Refrigeration, 98,238–248.